

**Manuscript version: Author's Accepted Manuscript**

The version presented in WRAP is the author's accepted manuscript and may differ from the published version or Version of Record.

**Persistent WRAP URL:**

<http://wrap.warwick.ac.uk/163012>

**How to cite:**

Please refer to published version for the most recent bibliographic citation information.

**Copyright and reuse:**

The Warwick Research Archive Portal (WRAP) makes this work by researchers of the University of Warwick available open access under the following conditions.

Copyright © and all moral rights to the version of the paper presented here belong to the individual author(s) and/or other copyright owners. To the extent reasonable and practicable the material made available in WRAP has been checked for eligibility before being made available.

Copies of full items can be used for personal research or study, educational, or not-for-profit purposes without prior permission or charge. Provided that the authors, title and full bibliographic details are credited, a hyperlink and/or URL is given for the original metadata page and the content is not changed in any way.

**Publisher's statement:**

Please refer to the repository item page, publisher's statement section, for further information.

For more information, please contact the WRAP Team at: [wrap@warwick.ac.uk](mailto:wrap@warwick.ac.uk).

# A white dwarf accreting planetary material determined from X-ray observations

Tim Cunningham<sup>1,2,\*</sup>, Peter J. Wheatley<sup>1,2</sup>, Pier-Emmanuel Tremblay<sup>1,2</sup>, Boris T. Gänsicke<sup>1,2</sup>, George W. King<sup>3</sup>, Odette Toloza<sup>4,5</sup> & Dimitri Veras<sup>1,2</sup>

<sup>1</sup>*Department of Physics, The University of Warwick, Coventry, CV4 7AL, UK*

<sup>2</sup>*Centre for Exoplanets and Habitability, University of Warwick, Gibbet Hill Road, Coventry, CV4 7AL, UK*

<sup>3</sup>*Department of Astronomy, University of Michigan, Ann Arbor, MI 48109, USA*

<sup>4</sup>*Departamento de Física, Universidad Técnica Federico Santa María, Av. España 1680, Valparaíso, Chile*

<sup>5</sup>*Millennium Nucleus for Planet Formation (NPF), Valparaíso, Chile*

**The atmospheres of a large proportion of white dwarf stars are polluted by heavy elements<sup>1</sup> that are expected to sink out of visible layers on short timescales<sup>2,3</sup>. This has been interpreted as a signature of ongoing accretion of debris from asteroids<sup>4</sup>, comets<sup>5</sup>, and giant planets<sup>6</sup>. This scenario is supported by the detection of debris discs<sup>7</sup> and transits of planetary fragments<sup>8</sup> around some white dwarfs. However, photospheric metals are only indirect evidence for ongoing accretion, and the inferred accretion rates and parent body compositions heavily depend on models of diffusion and mixing processes within the white dwarf atmosphere<sup>9–11</sup>. Here we report a  $4.4\sigma$  detection of X-rays from a polluted white dwarf, G29–38. From the measured X-ray luminosity, we derive an instantaneous accretion rate of**

$\dot{M}_X = 1.63_{-0.40}^{+1.29} \times 10^9 \text{ g s}^{-1}$ , **which is independent of stellar atmosphere models. This rate is higher than estimates from past studies of the photospheric abundances of G29–38, suggesting that convective overshoot may be needed to model the spectra of debris-accreting white dwarfs. We measure a low plasma temperature of  $kT = 0.5 \pm 0.2 \text{ keV}$ , corroborating the predicted bombardment solution for white dwarfs accreting at low accretion rates<sup>12,13</sup>.**

G29–38 is among the 100 closest white dwarfs and has hence been subject to detailed studies across most wavelength ranges. Whereas the detection of an infrared excess was initially interpreted as being most likely the signature of a brown dwarf, an origin linked to circumstellar dust was discussed as well<sup>7,14</sup>. Subsequent ultraviolet (UV) spectroscopy revealed trace metals in the hydrogen atmosphere of the white dwarf<sup>15</sup>, which were interpreted as evidence for ongoing accretion from a compact dusty debris disk that formed from the tidal disruption of an asteroid<sup>16</sup>. Assuming the white dwarf atmosphere is in an equilibrium between accretion and gravitational settling leads to a predicted accretion rate<sup>17</sup> of  $6.5 \times 10^8 \text{ g s}^{-1}$ . There are now more than a thousand known metal-polluted white dwarfs<sup>18</sup>, yet the evidence for ongoing accretion remains circumstantial, based on atmospheric abundances.

White dwarf accretion should be accompanied with intense heating of the infalling material, sufficient to promote cooling via X-ray emission<sup>19</sup>. This has been observed directly for white dwarfs accreting from stellar companions<sup>12,13,19,20</sup>, but never for a white dwarf accreting planetary debris. An *XMM-Newton* observation of G29–38 resulted in a non-detection due to a nearby bright X-ray source, placing an upper limit<sup>21</sup> on the accretion rate of  $2 \times 10^9 \text{ g s}^{-1}$ . A handful of metal-

polluted white dwarfs have been subject to X-ray studies, resulting so far only in upper limits, rather than firm detections<sup>22</sup>.

G29–38 was observed with *Chandra*<sup>23</sup> ACIS-S in September 2020, with a total exposure time of 106.33 ks (see Extended Data Table 1 for details). The sky location of the X-ray photons is shown in Fig. 1. The data reduction utilised three standard *Chandra* science bands: soft (0.5–1.2 keV), soft+medium (0.5–2.0 keV) and broad (0.5–7.0 keV). Within 1 arcsec of our target, we detected five X-ray events, with one medium and four soft band events. Using a Bayesian approach we found the 68% confidence interval on the broad band source count rate to be  $(2.4\text{--}6.6) \times 10^{-5}$  counts per second (see Extended Data Table 4 for other bands).

Fig. 2 shows the sky location of the soft+medium band events, which are fully consistent with the  $1\sigma$  uncertainty on the position from the *Chandra* ACIS-S astrometry. We computed the probability of the observed events arising by chance. A standard aperture photometry approach (see Methods) revealed source counts of 4, 5, and 5, in the soft, soft+medium and broad bands, respectively, with measured backgrounds of 0.10, 0.21 and 0.57 counts per 1 arcsec aperture. Using the Poisson distribution we found the statistical significance of the source counts in the three bands to be  $4.62$ ,  $4.71$  and  $3.64\sigma$  (see Extended Data Table 2). Accounting for the astrometric uncertainty by centring the aperture on the detected source position (Fig. 2), and using a smaller radius of 0.5 arcsec, which is appropriate for soft sources in ACIS-S, increases the detection significance to  $5.65$ ,  $5.94$  and  $5.06\sigma$  in the three science bands, respectively.

As confirmation that the observed source counts originated from the target, and not a back-



ground source, we used a source detection algorithm (see Methods) to derive a sky density of sources at the depth of the ACIS-S observations. In the soft, soft+medium, and broad bands, this analysis resulted in 6, 24, and 32 sources, respectively, (excluding our target) setting the background source sky density over the whole image to  $\rho_{\text{sky}} = 2, 9$  and  $13 \times 10^{-5} \text{ arcsec}^{-2}$ . The detected sources comprise real astrophysical sources and spurious detections arising from background counts. Interpreting this as the probability of a chance alignment, we were able to confirm the source events originated from G29–38 at 4.1, 3.8 and  $3.7\sigma$ . Finally, we performed a Monte Carlo aperture photometry analysis (see Methods) where, in the soft band image, only 0.001% of test apertures retrieved four events, with none retrieving more than four, thus allowing chance alignment with a background source to be ruled out at  $4.4\sigma$ . We conclude that the four recorded events in the standard soft science band reveal a  $> 4\sigma$  detection of X-rays from G29–38.

The energies of the five recorded events within 1 arcsec of our target are all in the range 0.7–1.4 keV, with four below 1 keV. The detection of most photons below 1 keV strongly suggests that the X-ray emission spectrum is very soft, and thus emitted from a relatively low-temperature plasma. To determine the best-fitting plasma temperature,  $T_X$ , we initially adopted an optically-thin isothermal plasma model and tested three distinct sets of abundances: Solar, bulk Earth and the spectroscopically determined photospheric abundances of G29–38<sup>17</sup>. The plasma temperatures were consistent, with the photospheric abundances corresponding to  $kT_X = 0.49^{+0.17}_{-0.21} \text{ keV}$  (see Extended Data Table 5).

While no debris-accreting white dwarf has previously been detected at X-ray wavelengths,

X-ray detections of white dwarfs in binaries are common, as they have higher accretion rates. Our measured plasma temperature of 0.5 keV is much lower than for white dwarfs accreting from stellar companions, which typically accrete at  $\gtrsim 10^{16} \text{ g s}^{-1}$  and have plasma temperatures<sup>19</sup> in the range 5–50 keV. This result is robust because the sensitivity of the ACIS-S detector peaks between 1–6.5 keV (see Extended Data Fig. 3) and emission with the same luminosity at higher temperatures would have been readily detected. Measuring such a low plasma temperature points to a heating mechanism that is distinct from the strong stand-off shocks thought to heat the infalling material at higher accretion rates<sup>20</sup>, where a shock is formed above the stellar surface. Instead, at the low accretion rate we observe for G29-38, the accreting material may have insufficient density to establish a shock above the stellar surface, and the material may impact directly onto the white dwarf surface: the proposed “bombardment” solution<sup>12,13</sup>. For a white dwarf with the parameters of G29-38 (mass  $M_{\text{WD}} = 0.6 M_{\odot}$  and radius  $R_{\text{WD}} = 0.0129 R_{\odot}$ ) the plasma temperature arising from accretion in the bombardment scenario was predicted<sup>12</sup> (see their equation 9) to be  $kT_{\text{X}} \approx 0.6 \text{ keV}$ , consistent with our measured plasma temperature.

To determine the X-ray flux, we adopted a more physically-motivated spectral model that combines emission from an optically-thin plasma at a range of temperatures (a cooling-flow model; see Methods). Integrating the best-fit model over the ACIS-S passband we derive an X-ray flux of  $F_{\text{X}}(0.3\text{--}7.0 \text{ keV}) = 1.97^{+1.55}_{-0.48} \times 10^{-15} \text{ erg s}^{-1} \text{ cm}^{-2}$ . The distance to G29-38 ( $d = 17.53 \pm 0.01 \text{ pc}^{24}$ ) implies an X-ray luminosity of  $L_{\text{X}}(0.3\text{--}7.0 \text{ keV}) = 7.24^{+5.66}_{-1.76} \times 10^{25} \text{ erg s}^{-1}$ . This is many orders of magnitude lower than observed for white dwarfs accreting from main-sequence companions (typically  $L_{\text{X}} = 10^{29}\text{--}10^{33} \text{ erg s}^{-1}$ )<sup>19</sup>.

We estimate the instantaneous accretion rate using<sup>20</sup>

$$\dot{M}_X = \frac{2}{A} L_X \frac{R_{WD}}{GM_{WD}}, \quad (1)$$

where the factor two accounts for 50% of the emitted photons being directed back towards the star<sup>25</sup> and the constant  $A$  quantifies the fraction of the total accretion-induced luminosity carried in the observed band. To calculate the X-ray accretion rate from our observations, we take the limiting case that the total luminosity is equivalent to the observed X-ray luminosity ( $A = 1$ ). Fig. 3 shows the 68% confidence interval on the instantaneous accretion rate derived for the two plasma models (isothermal and cooling flow) and two debris abundances (bulk Earth and photospheric), across the range of uncertainty on the photospheric effective temperature of G29–38. Using Equation (1), the bulk Earth abundances and cooling flow model, we find the best-fit instantaneous accretion rate to be  $\dot{M}_X(0.3\text{--}7.0\text{ keV}) = 1.63_{-0.40}^{+1.29} \times 10^9 \text{ g s}^{-1}$ . This is currently the only direct measurement of the instantaneous accretion rate of any white dwarf accreting planetary debris, providing the only way to validate the indirect accretion rates derived for a large number of white dwarfs from photospheric abundance analyses.

The observations provide robust constraints on hard X-ray emission ( $>2.0\text{ keV}$ ) as the *Chandra* ACIS-S detector is most sensitive in the range 1.0–6.5 keV (see Extended Data Fig. 3), whereas appreciable emission is likely softwards of the ACIS-S bandpass ( $< 0.3\text{--}0.5\text{ keV}$ ). To estimate the flux carried at unobserved wavelengths we integrated the best-fit cooling flow model across the wider energy band 0.0136–100 keV (see Methods). We found the flux in the wider integration band to be  $F_X(0.0136\text{--}100\text{ keV}) = 4.34_{-1.72}^{+14.8} \times 10^{-15} \text{ erg s}^{-1} \text{ cm}^{-2}$ . This represents a flux increase of a factor  $2.2_{-0.9}^{+7.5}$  compared with the *Chandra* ACIS-S passband integration.

Cyclotron emission cooling might radiate some of the accretion-induced luminosity at radio wavelengths if the magnetic field is strong enough<sup>26,27</sup>. At the  $3\sigma$  upper limit on the magnetic field of G29–38 (1.5 kG<sup>22</sup>) we find the maximum accretion rate increase due to cyclotron emission to be a factor  $1.1^{+0.6}_{-0.1}$  (see Extended Data Fig. 4), and for magnetic fields less than  $\approx 1$  kG the predicted cyclotron cooling emission is negligible.

Accretion rates at metal-polluted white dwarfs are typically inferred indirectly from spectroscopic abundance measurements, using white dwarf atmospheric models to quantify the flux of metals moving through the photosphere<sup>3</sup>. The time-averaged accretion rate of G29–38 was previously inferred<sup>17,28</sup> to be  $\dot{M} = (5.0 \pm 1.3) \times 10^8$  and  $(6.5 \pm 1.6) \times 10^8 \text{ g s}^{-1}$ . Fig. 3 shows the X-ray accretion rates, and those derived from previous spectroscopic studies. Our observations establish an X-ray accretion rate which agrees to within a factor three of those derived via the spectroscopic method. Recent results from 3D radiation-hydrodynamic simulations predict an increase in accretion rate inferred from spectroscopic observations due to convective overshoot<sup>10</sup>. At the effective temperature of G29–38 ( $\approx 11,500$ – $12,000$  K), the increase is predicted to be a factor 3–4. Thus the 3D accretion rate is predicted to be  $\approx 2 \times 10^9 \text{ g s}^{-1}$ , which is a closer match to the best fitting X-ray accretion rate (see Fig. 3). The diffusion timescale is also predicted to increase from days to years, which is more consistent with the lack of time variability of metal lines in G29–38<sup>29</sup>.

1. Koester, D., Gänsicke, B. T. & Farihi, J. The frequency of planetary debris around young white dwarfs. *Astron. Astrophys.* **566**, A34 (2014).
2. Paquette, C., Pelletier, C., Fontaine, G. & Michaud, G. Diffusion coefficients for stellar plasmas. *Astrophys. J. Suppl.* **61**, 177–195 (1986).
3. Koester, D. Accretion and diffusion in white dwarfs. New diffusion timescales and applications to GD 362 and G 29-38. *Astron. Astrophys.* **498**, 517–525 (2009).
4. Zuckerman, B., Koester, D., Melis, C., Hansen, B. M. & Jura, M. The Chemical Composition of an Extrasolar Minor Planet. *Astrophys. J.* **671**, 872–877 (2007).
5. Xu, S. *et al.* The Chemical Composition of an Extrasolar Kuiper-Belt-Object. *Astrophys. J. Lett.* **836**, L7 (2017).
6. Gänsicke, B. T. *et al.* Accretion of a giant planet onto a white dwarf star. *Nature* **576**, 61–64 (2019).
7. Zuckerman, B. & Becklin, E. E. Excess infrared radiation from a white dwarf—an orbiting brown dwarf? *Nature* **330**, 138–140 (1987).
8. Vanderburg, A. *et al.* A disintegrating minor planet transiting a white dwarf. *Nature* **526**, 546–549 (2015).
9. Bauer, E. B. & Bildsten, L. Polluted White Dwarfs: Mixing Regions and Diffusion Timescales. *Astrophys. J.* **872**, 96 (2019).

10. Cunningham, T., Tremblay, P.-E., Freytag, B., Ludwig, H.-G. & Koester, D. Convective overshoot and macroscopic diffusion in pure-hydrogen-atmosphere white dwarfs. *Mon. Not. R. Astron. Soc.* **488**, 2503–2522 (2019).
11. Heinonen, R. A. *et al.* Diffusion Coefficients in the Envelopes of White Dwarfs. *Astrophys. J.* **896**, 2 (2020).
12. Kuipers, J. & Pringle, J. E. Comments on radial white dwarf accretion. *Astron. Astrophys.* **114**, L4–L6 (1982).
13. Woelk, U. & Beuermann, K. Temperature structure of a particle – heated magnetic atmosphere. *Astron. Astrophys.* **280**, 169–173 (1993).
14. Graham, J. R., Matthews, K., Neugebauer, G. & Soifer, B. T. The Infrared Excess of G29–38: A Brown Dwarf or Dust? *Astrophys. J.* **357**, 216 (1990).
15. Koester, D., Provencal, J. & Shipman, H. L. Metals in the variable DA G29-38. *Astron. Astrophys.* **320**, L57–L59 (1997).
16. Jura, M. A Tidally Disrupted Asteroid around the White Dwarf G29-38. *Astrophys. J. Lett.* **584**, L91–L94 (2003).
17. Xu, S., Jura, M., Koester, D., Klein, B. & Zuckerman, B. Elemental Compositions of Two Extrasolar Rocky Planetesimals. *Astrophys. J.* **783**, 79 (2014).
18. Coutu, S. *et al.* Analysis of Helium-rich White Dwarfs Polluted by Heavy Elements in the Gaia Era. *Astrophys. J.* **885**, 74 (2019).

19. Mukai, K. X-Ray Emissions from Accreting White Dwarfs: A Review. *Publ. Astron. Soc. Pacif.* **129**, 062001 (2017).
20. Patterson, J. & Raymond, J. C. X-ray emission from cataclysmic variables with accretion disks. I. Hard X-rays. *Astrophys. J.* **292**, 535–549 (1985).
21. Jura, M., Munro, M. P., Farihi, J. & Zuckerman, B. X-Ray and Infrared Observations of Two Externally Polluted White Dwarfs. *Astrophys. J.* **699**, 1473–1479 (2009).
22. Farihi, J. *et al.* Magnetism, X-rays and accretion rates in WD 1145+017 and other polluted white dwarf systems. *Mon. Not. R. Astron. Soc.* **474**, 947–960 (2018).
23. Weisskopf, M. C., Tananbaum, H. D., Van Speybroeck, L. P. & O’Dell, S. L. Chandra X-ray Observatory (CXO): overview. *Proc. SPIE* **4012**, 2–16 (2000).
24. Gaia Collaboration *et al.* Gaia Data Release 2. Summary of the contents and survey properties. *Astron. Astrophys.* **616**, A1 (2018).
25. Kylafis, N. D. & Lamb, D. Q. X-ray and UV radiation from accreting degenerate dwarfs. II. *Astrophys. J. Suppl.* **48**, 239–272 (1982).
26. Ghosh, P. & Lamb, F. K. Disk accretion by magnetic neutron stars. *Astrophys. J. Lett.* **223**, L83–L87 (1978).
27. Metzger, B. D., Rafikov, R. R. & Bochkarev, K. V. Global models of runaway accretion in white dwarf debris discs. *Mon. Not. R. Astron. Soc.* **423**, 505–528 (2012).

28. Farihi, J., Jura, M. & Zuckerman, B. Infrared Signatures of Disrupted Minor Planets at White Dwarfs. *Astrophys. J.* **694**, 805–819 (2009).
29. Debes, J. H. & López-Morales, M. A Second Look at the Metal Line Variability of G29-38. *Astrophys. J. Lett.* **677**, L43 (2008).
30. *Chandra* X-ray Center. The *Chandra* Proposers' Observatory Guide. <https://cxc.cfa.harvard.edu/proposer/POG/html/index.html> (2020). [Online; accessed 30-October-2021].



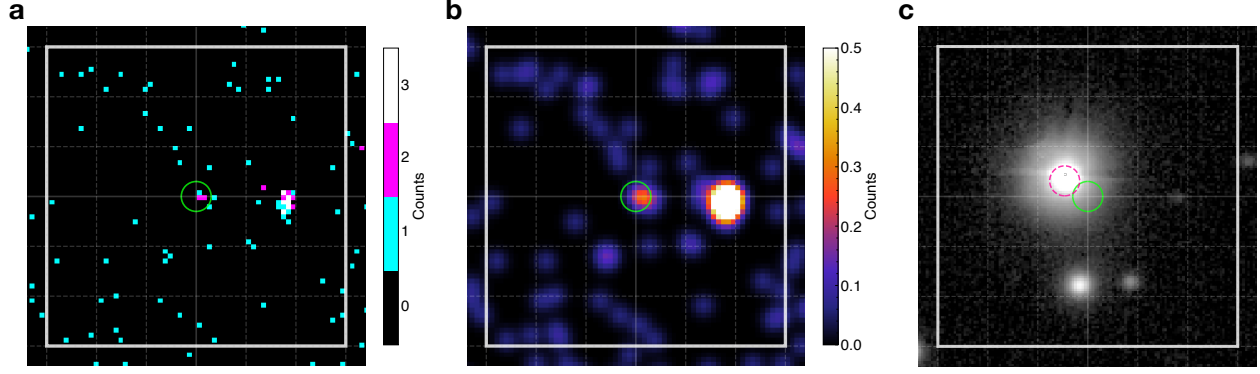


**Fig. 1 | X-ray and optical imaging of G29–38.** **a**, Image of the recorded events in the soft+medium (0.5–2.0 keV) band. Black, cyan, magenta and white represent 0, 1, 2, and 3 counts, respectively. **b**, The recorded events in the soft+medium (0.5–2.0) band convolved with the instrumental PSF. The PSF model used is a 2D Gaussian with a standard deviation of 0.81 arcsec, which is the mean PSF in the field of view shown, where the PSF varies by only  $\pm 1\%$ . **c**, The PanSTARRS1 (PS1) *i*-band image. In all panels, the white square, centered on the target coordinates, has sides of length 30 arcsec. The solid green circle shows 1.5 arcsec radius around target coordinates, whilst the dashed pink circle shows the target position at the PS1 epoch (J2014.89). The *Chandra* observations reveal a significant X-ray source at the expected position of G29–38.

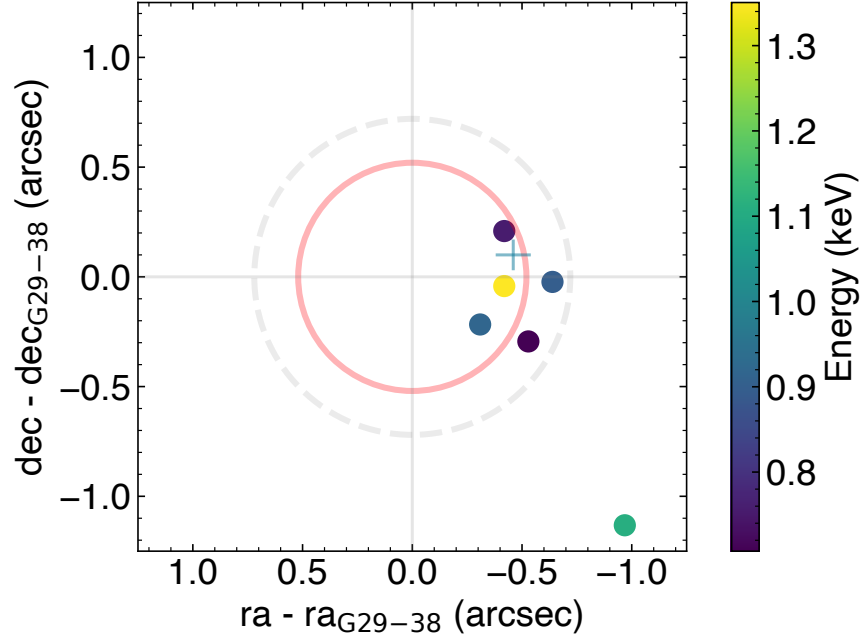


**Fig. 2 | Sky location of X-rays from G29–38.** Position of soft+medium band (0.5–2.0 keV) X-ray events in the merged observations. The colour of each event indicates the measured energy of the event. The red circle indicates the 68% positional uncertainty of 0.52 arcsec, arising from the astrometric accuracy of *Chandra* ACIS-S (see figure 5.4 of the *Chandra* Proposers’ Observatory Guide Version 23.0<sup>30</sup>) whilst the grey dashed circle indicates the 90% confidence limit of 0.72 arcsec. The five source photons used in our statistical analyses are all consistent with the expected sky location of G29–38. The blue cross indicates the expected offset derived from the only other *Gaia* EDR3 X-ray source in the ACIS-S field of view (see Extended Data Figure 1).

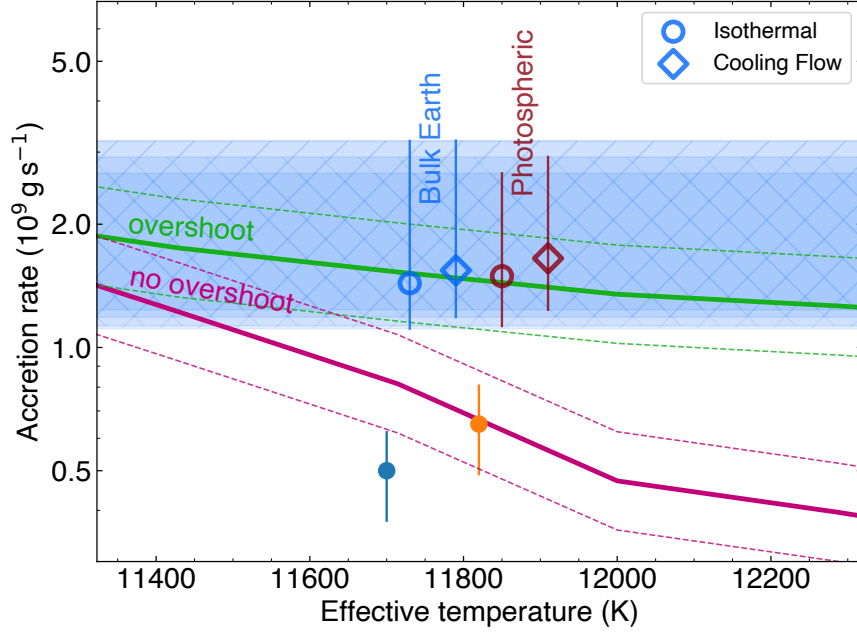


**Fig. 3 | Accretion rates inferred from the measured X-ray flux.** Accretion rates from the isothermal and cooling flow models are shown as open circles and diamonds, respectively. We show results for two plasma abundances; bulk Earth and photospheric<sup>17</sup> shown with blue and red, respectively. The filled horizontal bands show the 68% confidence interval on the four accretion rates, and for readability the 4 open data points are offset in effective temperature around 11 820 K. The X-ray accretion rates are computed using Equation (1). Using Equation (5), the accretion rates inferred from spectroscopic observations are shown in solid lines for a  $0.6M_{\odot}$  white dwarf, assuming bulk Earth composition; such that the observed calcium abundance<sup>17</sup> of  $\log [\text{Ca}/\text{H}] = -6.58 \pm 0.12$  makes up 1.6% of the accreted material. Accretion rates from models which include<sup>10</sup> or omit<sup>3</sup> convective overshoot mixing are shown in green or magenta, respectively, with  $1\sigma$  uncertainties (dashed lines) propagated from the spectroscopic abundance measurement. Also shown in solid circles are the previously published inferred accretion rates for G29–38 in blue<sup>28</sup>

and orange<sup>17</sup>.

## Methods

**Observations and data reduction.** Our observations consisted of five exposures using *Chandra* ACIS-S carried out between 22 and 27 September 2020. Each observation had an exposure time between  $\approx 15$ –25 ks (see Extended Data Table 1), with a total, merged exposure time of 106.33 ks, or 29.5 hr. All observations were carried out with the ACIS-S instrument using the *Gaia* DR2<sup>24</sup> proper motion-corrected coordinates of our target positioned on the S3 chip. The predicted X-ray luminosity was sufficiently low that our setup included the very faint mode which stores event grades in regions of  $5 \times 5$  pixels, rather than the standard  $3 \times 3$ . This allows an improved identification and rejection of background events, particularly at hard and very soft energies.

The data reduction was performed using the software package *Chandra* Interactive Analysis of Observations (CIAO<sup>31</sup>). The reduction began by reprocessing the five observations using the `chandra_repro` package with standard grade, status and good time filters and `vfaint` background cleaning applied. We employed `merge_obs` to merge the five observations into a single set of event files along with images, point spread function (PSF) maps and exposure maps. We performed this routine using combinations of the standard *Chandra* science energy bands: soft (0.5–1.2 keV), soft+medium (0.5–2.0 keV) and broad (0.5–7.0 keV). During each merging routine, the PSF maps and exposure maps were generated for each band with exposure evaluated on 0.9 keV, which represents an approximate mean of the suspected source photon energies.

**Statistical significance of detection** We initially investigate whether the detected events within 1 arcsec of our target amount to a statistically significant source. To determine the statistical signif-

ificance of the detection, we utilised the Poisson distribution, as appropriate for counting statistics with small numbers of events<sup>32</sup>. This allows us to quantify the confidence with which we can rule out the null hypothesis that we detected no source photons. We defined a source region of 1 arcsec around the coordinates of our target – Right Ascension and Declination of  $(352.196185 \pm 0.00004)^\circ$  and  $(+05.24686 \pm 0.00003)^\circ$ , respectively – which have been corrected to the J2020.73 epoch using the *Gaia* EDR3<sup>33</sup> astrometry. The nearby background region was defined as a circle with a 52 arcsec radius, avoiding obvious point sources – such as the nearby bright source which contaminated previous *XMM-Newton* observations<sup>22</sup> (e.g., see Extended Data Fig. 1; panels a–c) – as well as drops in sensitivity in the exposure map.

Extended Data Table 2 shows the source and background counts from the full, merged observation of 106.33 ks. The Poisson distribution gives the probability of receiving  $N$  or more counts, given an expected mean background,  $b$ , as

$$P(N|b) = \frac{b^N e^{-b}}{N!} . \quad (2)$$

We can therefore reject the null hypothesis that there are no source photons with a confidence level (CL) of  $CL = 100 \times (1 - P(N|b))$ . In the soft, soft+medium and broad bands, we find  $CL = 99.99962\%$ ,  $99.99975\%$ , and  $99.97255\%$ , respectively. The statistical significance,  $s$ , can be computed as

$$s = \text{erf}^{-1} (1 - P(N|b)) \sqrt{2}, \quad (3)$$

which for each of the three bands is  $s = 4.62$ ,  $4.71$ , and  $3.64\sigma$ , respectively. We note that adopting a smaller aperture with a radius of 0.5 arcsec, which is appropriate for soft sources with ACIS-S (see figure 6.10 of the *Chandra* Proposers’ Observatory Guide Version 23.0<sup>30</sup> where the enclosed

fractional power is  $>50\%$  for 0.5 arcsec apertures), and accounting for the astrometric uncertainty by centring the aperture on the locus of photons at the source position (see Fig. 2), increases the detection significance in the three science bands to  $5.65$ ,  $5.94$  and  $5.06\sigma$ , respectively. We conclude that in all three science bands considered, an X-ray source is detected at the expected position of our target, G29–38.

**Count rates and confidence intervals** For each science band considered, we converted the number of counts to a count rate using the total exposure time of 106.33 ks. In the soft, soft+medium and broad bands we find count rates of  $0.038^{+0.017}_{-0.022}$ ,  $0.047^{+0.020}_{-0.023}$  and  $0.047^{+0.024}_{-0.019}$   $\text{ks}^{-1}$  per 1 arcsec aperture, respectively. The 68% confidence interval on count rate across all three bands is  $(2.1\text{--}7.0) \times 10^{-5}$  counts per second, while the 90% confidence interval spans  $(1.3\text{--}9.0) \times 10^{-5}$  counts per second. The confidence intervals were calculated using a Bayesian approach to Poisson statistics, following methodology in ref.<sup>34</sup>. This uses a simple prior which requires a non-negative number of source counts.

**Investigating positional uncertainty** The five recorded soft+medium band events within 1 arcsec of our target coordinates have a sky position which is shifted by approximately  $-0.5$  arcsec in right ascension. In Fig. 2 we plot the sky position of the recorded events in the soft+medium band within 1.1 arcsec of our target. We find that all five of the photons in the soft+medium bands have sky locations consistent with the  $1\sigma$  uncertainty on the target’s position, which arises from the astrometric uncertainty of the telescope itself. From figure 5.4 of the *Chandra* Proposers’ Observatory Guide (Version 23.0)<sup>30</sup>, the 68% confidence limit on the radial offset of a given target is 0.52 arcsec. This value was computed for observations between 2015–2020, by comparing the

radial offset of *Chandra* sources with optical sources predominantly from the Tycho-2 catalog. The thick, red ellipse in Fig. 2 shows the 68% confidence interval on the position of our target and illustrates the expected precision of the target position in our data. We find that all five events considered in our earlier statistics fall within this area.

**Constraining source positional offset** The center of the five photons attributed to our source exhibit an apparent offset compared to the *Gaia* EDR3 position of approximately  $-0.5$  arcsec in RA. The mean coordinates, in (RA, DEC), of the five photons from the merged observations are  $(352.19606 \pm 0.00004, +5.24684 \pm 0.00005)^\circ$ . Compared to the *Gaia* EDR3 expected position of our target, this represents an offset of  $(-0.51 \pm 0.13, -0.07 \pm 0.17)$  arcsec. To investigate the cause for this offset we searched for optical counterparts in the full ACIS-S CCD image, finding one additional X-ray source with a counterpart in *Gaia* EDR3. To identify counterparts in *Gaia* EDR3, a positional cross-match was performed, searching for sources within 5 arcsec of the sources detected with the source detection algorithm `wavdetect`<sup>35</sup> (see next section and Extended Data Fig. 1) in the merged image for all three science bands (see Extended Data Table 3). Excluding our target, the cross-match resulted in one *Gaia* EDR3 source with source ID 2661110815469507072. Corrected for proper motion, the expected coordinates of this source at the epoch of observation (J2020.73) are  $(352.18248533 \pm 0.00000007, +5.34150200 \pm 0.00000008)^\circ$ . The output of `wavdetect` gives the coordinates for the center of the detected source  $(352.182358 \pm 0.000022, +5.341529 \pm 0.000020)^\circ$ . This leads to a positional offset between the *Gaia* EDR3 proper-motion-corrected position and the center of the detected source in `wavdetect` of  $(-0.46 \pm 0.08, +0.10 \pm 0.07)$  arcsec which is consistent with the offset observed



for our target. This offset can be seen in Extended Data Fig. 1 where the *Gaia* position is shown in white and the `wavdetect` source is shown in cyan. The offset observed for our target and the only other *Gaia* source in the field are fully consistent to within  $1\sigma$ , as can be seen in Fig. 2.

**Ruling out background contamination** To determine the probability of chance alignment with a background source we follow two methodologies. In the first, we run a source-detection algorithm to provide an independent constraint on the number of sources at this depth of pointing. We rely upon `wavdetect`<sup>35</sup>, a wavelet-based algorithm included in the CIAO package, designed for the spatial analysis of Poisson count data. As recommended in the documentation we set the `sigthresh` parameter, which defines the threshold for identifying a pixel as belonging to a source, to  $1/n_{\text{px}} \approx 10^{-6}$ , which implies that approximately one identified source will be a false detection. We perform this analysis in all three of the standard bands considered in this study, as well as for two values of `sigthresh`,  $s_1$  and  $s_2$ . In the first, we use  $s_1 = 10^{-6}$ , which is the recommended value for the number of pixels ( $1024 \times 1024$ ) of the S3 CCD. The second, more stringent, value of `sigthresh`,  $s_2 = 5 \times 10^{-7}$ , accounts for the ‘dead’ corners of the image which arise from aligning the CCD image with the world coordinate system (WCS). This results in an image with  $1414 \times 1401$  pixels. The results are given in Extended Data Table 3, and Extended Data Fig. 1 shows the sky location of the detected sources in all three science bands. Across the entire CCD image we detect 7, 25 and 32 sources, in the soft, soft+medium and broad bands, respectively. We find our target is not detected in the broad band image, regardless of the `sigthresh` value. In the soft band, the target is detected at the higher `sigthresh` value, but not with the more stringent value. And in the soft+medium band we find the source is detected in both cases. Dividing the total

number of sources in each band by the field of view ( $1024^2 \times 0.4920^2 \text{ arcsec}^2$ ) reveals sky densities of 2.76, 9.85 and  $12.6 \times 10^{-5} \text{ arcsec}^{-2}$ , in the soft, soft+medium and broad bands, respectively. To estimate the probability of chance alignment with a background source we multiple the sky density by an effective location error area. For this area we adopt the 90% confidence limit on the radial offset of ACIS-S targets, which is given as 0.72 arcsec (see figure 5.4 of the *Chandra* Proposers' Observatory Guide Version 23.0<sup>30</sup>). We can thus rule out chance alignment at a significance of  $\text{erf}^{-1}(1 - \pi 0.72^2 \rho_{\text{sky}}) \sqrt{2} = 4.1, 3.8 \text{ and } 3.7\sigma$ , or confidence of 99.996, 99.985 and 99.979%, respectively

To further test this result, we performed a Monte Carlo aperture photometry experiment. We placed 100,000 apertures with 1 arcsec radii within 100 arcsec of the target. This area was chosen to confine the study to the region of the ACIS-S3 CCD where the PSF does not exhibit a significant gradient, as beyond  $\approx 120 \text{ arcsec}$  the PSF increases significantly. This effect can be seen in the output of the `wavdetect` algorithm in the top panels of Extended Data Fig. 1, where the sources detected near the edge of the CCD appear to be much larger. For the Monte Carlo aperture photometry test we make use of the Python package `scipy`<sup>36</sup>, in particular the `KDTree` module. This facilitates the rapid comparison of a large number of test aperture positions with those of recorded events from our observation. To estimate the true sky density of background sources we exclude the target and known nearby bright source using circular masks of radius 1 arcsec and 2.5 arcsec, respectively. The final number of test apertures was slightly reduced after the removal of the  $\approx 150\text{--}200$  which fell within masked regions.

The results of this test on the soft and soft+medium band events are shown in Extended

Data Fig. 2. In the soft band analysis, we find 1 in 99,828 test apertures (0.001%) retrieved four counts, while no test apertures found more than four counts. This allows us to rule out chance alignment with a background source at a significance of  $4.4\sigma$ . In the soft+medium band, we find 56 in 99,852 test apertures (0.056%) have five or more counts, while 48 (0.048%) returned between 6–27 counts, allowing us to rule out chance alignment at the  $3.4\sigma$  level. The reason the chance-alignment significance is lower in the soft+medium band is not because there is any doubt about the source detection, but because (1) our source has a soft spectrum and so contributes little flux in the medium band, and (2) there are a much larger number of background sources in the medium band, since most X-ray sources are harder than our target, and because the effective area of the telescope is higher. This test also provides an empirical confirmation of the quoted expected backgrounds in Extended Data Table 2, with fewer than 10% and 20% of 1 arcsec test apertures returning any counts in the soft and soft+medium bands, respectively.

We have shown that the counts detected within 1 arcsec of our target coordinates allow the rejection of the null hypothesis – that no source counts were measured – with a conservative confidence of 99.97255–99.99962% ( $3.64$ – $4.71\sigma$ ). Using the recommended aperture size of 0.5 arcsec, and centring the aperture on the observed source position, we find the source significance increases to  $5.06$ – $5.91\sigma$ . We have also shown that the observed position of the five recorded events is consistent with the expected position of our target, to within the  $1\sigma$  astrometric uncertainty, further confirmed by comparison to the only other observed X-ray source with a *Gaia* EDR3 counterpart. We have tested the hypothesis that recorded source counts could have originated instead from a background source, and by constraining the sky density of sources at this depth of pointing us-

ing `wavdetect`, we rule out a chance alignment with a background source at a confidence of 99.996 and 99.985% ( $4.1$  and  $3.8\sigma$ ) in the soft and soft+medium bands, respectively. Confirming these results with Monte Carlo aperture photometry, in the soft band, with 0.001% of test apertures returning four counts, chance alignment can be ruled out with a confidence of 99.999% ( $4.4\sigma$ ). Given the high degree of confidence to which the observed events can be attributed to our target, G29–38, in the following we perform spectral modelling to derive an X-ray flux, luminosity and accretion rate.

**Spectral model and debris composition** We perform a spectral analysis assuming two different optically-thin plasma models, and three distinct abundance profiles. The first model is a one-component, isothermal plasma implemented in the `vvapec` model within the `XSPEC` software package (version 12.11.1),<sup>37</sup> which uses the AtomDB atomic database<sup>38</sup>. The second model, `mkcflow`, is a cooling flow model that allows for a range of temperatures, with the relative emission measure for each temperature weighted by the inverse of its emissivity. We selected the option to use the AtomDB database. This cooling flow model is more physically-motivated than the isothermal model and is likely to provide a better estimate of the X-ray flux beyond the observed bandpass. We fitted the `mkcflow` model by fixing the lowest temperature plasma at the lower limit of the model of  $kT = 0.08$  keV, only allowing the upper temperature of the range to vary, enabling a one-parameter fit. This models the emission from material heated to the upper temperature and then cooling to temperatures lower than can be detected with *Chandra* ACIS-S. The three abundance profiles we use are Solar<sup>39</sup>, bulk Earth<sup>40</sup>, and the observed photospheric metal abundances<sup>17</sup> of G29–38 with an equal number abundance of hydrogen. The composition of the infalling mate-

rial is best described as a rocky, water-depleted, chondritic object<sup>17</sup>, with detected lithophile (O, Si, Mg, Ca, Ti, and Cr), siderophile (Fe), and atmophile (C) elements. If the heated plasma is formed sufficiently close to the stellar surface, such as in the bombardment scenario, the rocky accreted material may be mixed with photospheric hydrogen. However, we found that our results were not sensitive to the hydrogen abundance, as at the best-fit plasma temperatures ( $\approx 0.5$  keV) the cooling is dominated by metal line emission. At the distance to G29–38, the interstellar column density is expected<sup>41</sup> to be only around  $N_{\text{H}} = 5.4 \times 10^{18} \text{ cm}^{-2}$ , which has a negligible effect in the *Chandra* ACIS-S passband ( $< 0.5\%$  absorption at 0.5 keV). The five events in the ACIS-S spectrum were fitted unbinned, using the C-statistic,<sup>42</sup> and with no background subtraction.

Extended Data Figure 3 shows the spectral fits and Extended Data Table 5 shows the best-fit plasma temperatures for all six models, as well as the 68% and 90% confidence intervals. The bulk Earth and photospheric models agree to within the 68% confidence interval. The observed photospheric abundances of G29–38 could be scaled by the microscopic diffusion timescale in the atmosphere to infer a more accurate accreted debris composition. The difference, however, would be small, and the agreement between the bulk Earth and photospheric models strongly suggests that the observations would not be sensitive to such a correction.

**Deriving X-ray Flux** We derive a total flux due to accretion by integrating the best-fit spectral models over a finite frequency (or energy) range. We find a robust lower limit on the X-ray flux of  $F_{\text{X}}(0.3\text{--}7.0 \text{ keV}) = 1.97_{-0.48}^{+1.55} \times 10^{-15} \text{ erg s}^{-1} \text{ cm}^{-2}$  by performing the integration only over the energies within the *Chandra* ACIS-S passband (0.3–7.0 keV). We also perform the integration across a slightly narrower band (0.5–7.0 keV) as the instrument sensitivity below 0.5 keV has degraded

since launch and is now relatively low. These results, with their associated confidence intervals, are shown in Extended Data Table 6. With the lower limit on X-ray flux tightly constrained, providing an upper limit on the X-ray flux is more challenging. This is primarily due to the lack of observations between the very soft X-rays ( $\sim 0.1$  keV) and the UV. There are no instruments currently equipped to perform observations at these Extreme Ultraviolet (EUV) wavelengths, so directly measuring the flux in this regime is, for now, impossible. The constant  $A$  included in Equation (1) describes the predicted fraction of the total luminosity carried in the *Chandra* ACIS-S passband. Previous studies<sup>20,21</sup> have made the approximation that  $A = 0.5$ , or  $0.25$ . We provide an upper estimate of the X-ray and EUV flux by integrating the best-fit spectral models over a much wider energy range (0.0136–100.0 keV). Model spectra over this broadband are plotted in Extended Data Fig. 3 and we include fluxes calculated for this broad band in Extended Data Table 6.

Extended Data Fig. 3 shows the X-ray flux computed in the three integration bands used in this analysis. For clarity, from here onwards we show results only from the cooling flow model (`mkcflow`) using the photospheric abundances. The use of the cooling flow model is designed to provide a realistic temperature distribution and hence realistic fluxes in the EUV band (it can be compared with the isothermal model in Extended Data Fig. 3). From left to right in Extended Data Fig. 3 the size of the integration domain increases, and as expected the best-fit X-ray flux (and thus accretion rate) also increases, with the widest band (0.0136–100 keV) providing an upper estimate of the X-ray and EUV flux. The wider integration band results in a best-fit accretion rate which is  $2.2^{+7.5}_{-0.9}$  times higher than that derived from the ACIS-S passband, where the errors represent the 68% confidence interval. We note that the 68% and 90% upper bounds on the fluxes increase by a

factor  $\sim 10$  and  $\sim 100$ , respectively, due to the uncertain importance of the EUV band.

**X-ray luminosity** We derive an X-ray luminosity from the X-ray flux measured in the previous section using  $L_X = 4\pi d^2 F_X$  with the distance to G29–38 of  $d = (17.53 \pm 0.01)$  pc calculated from the *Gaia* EDR3 parallax. Extended Data Table 6 shows the best-fit X-ray luminosity for each of the energy ranges. From the robust lower limit on the X-ray flux, the best-fit X-ray luminosity from our observations is found to be  $L_X(0.3 - 7.0 \text{ keV}) = 7.24^{+5.66}_{-1.76} \times 10^{25} \text{ erg s}^{-1}$ , where the errors are indicative of the 68% confidence interval.

**X-ray accretion rates** Here we estimate the instantaneous accretion rate using a simple model which has been employed in studies of accreting white dwarfs<sup>20–22</sup>. In this model, infalling material reaches near-free fall velocity, forming a heated plasma as the material approaches the white dwarf surface<sup>19</sup>. The plasma must radiate outwards a total energy equivalent to the initial gravitational potential energy of the accreted material such that<sup>20</sup>

$$L_{\text{tot}} = \frac{1}{2} \frac{GM_{\text{WD}}\dot{M}}{R_{\text{WD}}}, \quad (4)$$

where  $R_{\text{WD}}$  is the white dwarf radius, at which infalling material impacts the atmosphere, and the factor  $1/2$  accounts for 50% of emitted photons being directed back towards and absorbed by the star<sup>20,25</sup>. We allow the emitting plasma to be formed by individual atoms reaching the white dwarf atmosphere in a scenario termed the “bombardment” solution, relevant for low accretion rate systems,<sup>12,13</sup> such that the X-ray emitting plasma is formed at the white dwarf radius ( $R_{\text{WD}} = 0.0129 R_{\odot}$ ). This scenario was hypothesised for white dwarfs accreting from main-sequence companions at low accretion rates, and predicts a plasma temperature ( $\approx 0.6 \text{ keV}$ ) com-

parable to that which we have measured from our observations (0.5 keV). From the total luminosity, the X-ray luminosity can be written  $L_X = AL_{\text{tot}}$ , where the constant  $A$  accounts for the fraction of the flux emitted outside the observed passband. If the plasma cooling is entirely mediated by line cooling in the observed X-ray passband (0.3–7.0 keV), then  $A = 1$ . If the plasma experiences additional line cooling at harder, or softer energies than those observed, then  $A < 1$ . If the plasma cools via other physical mechanisms, such as cyclotron emission cooling, then some of the total luminosity will be radiated at radio wavelengths, in which case  $A < 1$ . This has typically been set to  $A = 0.25\text{--}0.5$  in previous X-ray studies<sup>20,21</sup>. The flux integration over the wider energy band (0.0136–100 keV) allowed us to constrain the increase due to unobserved flux to a factor  $2.2^{+7.5}_{-0.9}$ , which corresponds to  $A = 0.5^{+0.3}_{-0.4}$ , consistent with estimates from previous studies for white dwarfs accreting from main-sequence companions, with errors corresponding to the 68% confidence interval.

The accretion rate can be inferred from the *Chandra* ACIS-S observations using Equation (1), which describes an accretion flow converting its gravitational potential energy into an X-ray luminosity. In Extended Data Table 6 we use this equation in the limiting case, with all X-ray flux emitted within the *Chandra* ACIS-S passband ( $A = 1$ ) to transform the X-ray luminosities into accretion rates. We find the X-ray accretion rate, measured from our observations, to be  $\dot{M}_X(0.3\text{--}7.0\text{ keV}) = 1.63^{+1.29}_{-0.40} \times 10^9 \text{ g s}^{-1}$ . The true accretion rate could be inferred to be higher for two reasons: firstly, there may be additional flux carried at lower, unobserved energies, and secondly, there could be some contribution if the magnetic field is sufficiently high to promote some cooling via cyclotron emission cooling<sup>22</sup>. We have constrained the first consideration by in-



tegrating the best-fit model spectra over the full EUV and X-ray regime, finding the flux to increase by up to a factor  $2.2^{+7.5}_{-0.9}$ , or  $A = 0.5^{+0.3}_{-0.4}$ . We will consider the possible increase in accretion rate due to cyclotron emission cooling in the following.

A magnetic field on G29–38 has the potential of funneling the accretion flow towards the magnetic poles of the white dwarf<sup>26,27</sup>, and if the density in the post-shock region is sufficiently high, cyclotron emission at radio wavelengths could contribute to its cooling, which would imply that the accretion rate based on the X-ray data is underestimated. An estimate for the temperature,  $T_B$ , above which cyclotron emission cooling dominates was given by equation 10 from ref.<sup>22</sup> such that one can approximate the total luminosity to be  $L_{\text{tot}} \approx (T_X/T_B)L_X$  for a thermal plasma with temperature  $T_X$ . The  $3\sigma$  upper limit on the magnetic field of G29–38 which was found to be 1.5 kG from spectropolarimetry observations with FORS2<sup>22</sup>, and even if the magnetic field of G29–38 is close to the observational detection limit, the maximum correction due to cyclotron emission cooling is predicted to be a factor  $1.1^{+0.6}_{-0.1}$  given the observed X-ray accretion rate (see Extended Data Fig. 4). And for magnetic fields less than  $\approx 1$  kG negligible cyclotron cooling emission is predicted. In summary, compared to the X-ray accretion rate measured in the ACIS-S passband,  $\dot{M}_X = 1.63^{+1.29}_{-0.40} \times 10^9 \text{ g s}^{-1}$ , the true accretion rate could be higher by a factor  $1.1^{+0.6}_{-0.1}$  due to possible cyclotron radiation and a factor  $2.2^{+7.5}_{-0.9}$  due to additional flux emitted at unobserved wavelengths (see Methods and Extended Data Table 6). Combining both possibilities for an increase in accretion rate by multiplying the two factors together, the upper estimate on the true accretion rate could be a factor  $2.4^{+14.1}_{-1.1}$  higher than the observed X-ray accretion rate, where the errors represent the 68% confidence interval.

**Atmospheric parameters** G29–38 was identified as a metal-polluted, hydrogen atmosphere (DAZ) white dwarf<sup>15</sup>. It is also a pulsating, or ZZ Ceti, star with large-amplitude non-radial pulsations with periods on the time scale  $t \approx 110 - 1250$  s<sup>43,44</sup>. From fitting the broadband energy distribution<sup>45,46</sup>, the effective temperature of G29–38 has been estimated to be  $T_{\text{eff}} = (11529 \pm 206)$  K and  $(12090 \pm 229)$  K, when using *Gaia* EDR3 and PanSTARRS1 (PS1) photometry, respectively. From the *Gaia* EDR3 parallax, the mass was found to be  $M = (0.629 \pm 0.016) M_{\odot}$  and  $(0.670 \pm 0.017) M_{\odot}$ , when using *Gaia* EDR3 and PS1 photometry, respectively. This spans the full range of effective temperatures previously derived for this star using the spectroscopic method to fit the Balmer absorption lines<sup>15,17,28,47</sup>. Using the observed Balmer line spectrum time-averaged over multiple pulsation cycles<sup>47</sup> and the latest model spectra<sup>48</sup> with 3D corrections<sup>49</sup> we obtain  $T_{\text{eff}} = (11906 \pm 190)$  K and  $M = (0.689 \pm 0.031) M_{\odot}$ . The model accretion rates (solid lines) derived in Fig. 3 are plotted over an x-axis range to include both the EDR3 and PS1 effective temperatures, for a H-atmosphere white dwarf with a mass of  $M = 0.60 M_{\odot}$ . Radiation-hydrodynamic simulations of convective overshoot are currently only available for H-atmosphere white dwarfs with surface gravities of  $\log g = 8.0$  ( $M_{\text{WD}} = 0.6 M_{\odot}$ ). For self-consistency, the calculation of X-ray accretion rates (Equation 1) and spectroscopic accretion rates (Equation 5) use the canonical white dwarf mass of  $M_{\text{WD}} = 0.6 M_{\odot}$ . This is 3–15% smaller than the mass of G29–38 derived from photometric and spectroscopic fits ( $M_{\text{WD}} = 0.629\text{--}0.670 M_{\odot}$ ). Given that the X-ray accretion rate scales proportionally with white dwarf mass, this represents only a small (3–15%) uncertainty in the measured accretion rate.

**Spectroscopic accretion rates** In the accretion-diffusion scenario, under the steady-state assumption, an accretion rate can be inferred from spectroscopic observations as<sup>3</sup>

$$\dot{M}_i = X_i \frac{M_{\text{cvz}}}{t_{\text{diff},i}}, \quad (5)$$

where  $X_i$  is the photospheric abundance of element  $i$ ,  $M_{\text{cvz}}$  is the convectively-mixed mass and  $t_{\text{diff},i}$  is the diffusion timescale set by the microscopic physics at the base of the mixed surface layers. From spectroscopic observations and model atmosphere analyses, the time-averaged accretion rate of G29–38 has previously been inferred<sup>17,28</sup> to be  $\dot{M} = (5.0 \pm 1.3) \times 10^8$  and  $(6.5 \pm 1.6) \times 10^8 \text{ g s}^{-1}$ . The uncertainty on the first value<sup>28</sup> was given as a typical 25% uncertainty (0.1 dex) on the spectroscopically measured calcium abundance. The error on the second value<sup>17</sup> was also estimated in the same way. Our observations establish an X-ray accretion rate which agrees to within a factor 3 of previously derived spectroscopic accretion rates. The key parameters in the determination of a spectroscopic accretion rate are the observed spectroscopic metal abundance, the convectively-mixed mass at the surface, and diffusion timescale at the base of the mixed region (see Equation 5 in Methods). Using the measured calcium abundance as a proxy for bulk Earth composition, we calculated the 1D spectroscopic accretion rate with diffusion coefficients from ref.<sup>50</sup> across the range of temperatures found in the literature for G29–38 (see Fig. 3). Recent results from 3D radiation-hydrodynamic simulations predict that the convectively-mixed mass can increase by up to 2.5 orders of magnitude when accounting for enhanced mixing due to convective overshoot<sup>10,51,52</sup>, whilst the diffusion timescale can increase by up to 1.5 dex. This leads to a temperature-dependent increase in accretion rate inferred from spectroscopic observations due to convective overshoot<sup>10</sup>. At the effective temperature of G29–38 ( $\approx 11,500\text{--}12,000 \text{ K}$ ), convec-

tive overshoot is predicted to increase the accretion rate by a factor 2–4. Thus the 3D accretion rate is predicted to be  $\approx 2 \times 10^9 \text{ g s}^{-1}$ , which is in close agreement with the derived X-ray accretion rate (see Fig. 3).

**Data Availability** The data that support the plots within this paper and other findings of this study are available from the *Chandra Data Archive*. The observation ID numbers are given in Extended Data Table 1.

**Code Availability** The official *Chandra* reduction software package CIAO – which includes `merge_obs`, `wavdetect` and `XPSEC` – is freely and publicly available (`cxc.cfa.harvard.edu/ciao/`). So too is the Python package `scipy`.

31. Fruscione, A. *et al.* CIAO: Chandra’s data analysis system. *Proc. SPIE* **6270**, 62701V (2006).
32. Li, T. P. & Ma, Y. Q. Analysis methods for results in gamma-ray astronomy. *Astrophys. J.* **272**, 317–324 (1983).
33. Gaia Collaboration *et al.* Gaia Early Data Release 3. Summary of the contents and survey properties. *Astron. Astrophys.* **649**, A1 (2021).
34. Kraft, R. P., Burrows, D. N. & Nousek, J. A. Determination of Confidence Limits for Experiments with Low Numbers of Counts. *Astrophys. J.* **374**, 344 (1991).
35. Freeman, P. E., Kashyap, V., Rosner, R. & Lamb, D. Q. A Wavelet-Based Algorithm for the Spatial Analysis of Poisson Data. *Astrophys. J. Suppl.* **138**, 185–218 (2002).
36. Virtanen, P. *et al.* SciPy 1.0: Fundamental Algorithms for Scientific Computing in Python. *Nat. Methods* **17**, 261–272 (2020).
37. Arnaud, K. A. XSPEC: The First Ten Years. *Astron. Soc. Pac. Conf. Ser.* **101**, 17 (1996).
38. Foster, A. R., Ji, L., Smith, R. K. & Brickhouse, N. S. Updated Atomic Data and Calculations for X-Ray Spectroscopy. *Astrophys. J.* **756**, 128 (2012).
39. Asplund, M., Grevesse, N., Sauval, A. J. & Scott, P. The Chemical Composition of the Sun. *Annu. Rev. Astron. Astrophys.* **47**, 481–522 (2009).
40. McDonough, W. F. & Sun, S. s. The composition of the Earth. *Chem. Geol.* **120**, 223–253 (1995).

41. Redfield, S. & Linsky, J. L. The Three-dimensional Structure of the Warm Local Interstellar Medium. II. The Colorado Model of the Local Interstellar Cloud. *Astrophys. J.* **534**, 825–837 (2000).
42. Cash, W. Parameter estimation in astronomy through application of the likelihood ratio. *Astrophys. J.* **228**, 939–947 (1979).
43. Patterson, J., Zuckerman, B., Becklin, E. E., Tholen, D. J. & Hawarden, T. The Infrared and Optical Pulsations of G29-38. *Astrophys. J.* **374**, 330 (1991).
44. Kleinman, S. J. *et al.* Understanding the Cool DA White Dwarf Pulsator, G29-38. *Astrophys. J.* **495**, 424–434 (1998).
45. McCleery, J. *et al.* Gaia white dwarfs within 40 pc II: the volume-limited Northern hemisphere sample. *Mon. Not. R. Astron. Soc.* **499**, 1890–1908 (2020).
46. Gentile Fusillo, N. P. *et al.* A catalogue of white dwarfs in Gaia EDR3. *arXiv e-prints* arXiv:2106.07669 (2021).
47. Gianninas, A., Bergeron, P. & Ruiz, M. T. A Spectroscopic Survey and Analysis of Bright, Hydrogen-rich White Dwarfs. *Astrophys. J.* **743**, 138 (2011).
48. Tremblay, P. E. & Bergeron, P. Spectroscopic Analysis of DA White Dwarfs: Stark Broadening of Hydrogen Lines Including Nonideal Effects. *Astrophys. J.* **696**, 1755–1770 (2009).
49. Tremblay, P.-E., Ludwig, H.-G., Steffen, M. & Freytag, B. Spectroscopic analysis of DA white dwarfs with 3D model atmospheres. *Astron. Astrophys.* **559**, A104 (2013).

50. Koester, D., Kepler, S. O. & Irwin, A. W. New white dwarf envelope models and diffusion. Application to DQ white dwarfs. *Astron. Astrophys.* **635**, A103 (2020).
51. Freytag, B., Ludwig, H.-G. & Steffen, M. Hydrodynamical models of stellar convection. The role of overshoot in DA white dwarfs, A-type stars, and the Sun. *Astron. Astrophys.* **313**, 497–516 (1996).
52. Kupka, F., Zaussinger, F. & Montgomery, M. H. Mixing and overshooting in surface convection zones of DA white dwarfs: first results from ANTARES. *Mon. Not. R. Astron. Soc.* **474**, 4660–4671 (2018).



**Author Correspondence** All correspondence regarding this work should be directed to T. Cunningham (email: [timothy.cunningham@warwick.ac.uk](mailto:timothy.cunningham@warwick.ac.uk)).

**Acknowledgements** This research was supported by a Leverhulme Trust Grant (ID RPG-2020-366). PJW, BTG and PET were supported by the UK STFC consolidated grant ST/T000406/1. PET received funding from the European Research Council under the European Union’s Horizon 2020 research and innovation programme number 677706 (WD3D). BTG was supported by a Leverhulme Research Fellowship, OT was supported by a Leverhulme Trust Research Project Grant and FONDECYT project 32103, and DV gratefully acknowledges the support of the STFC via an Ernest Rutherford Fellowship (grant ST/P003850/1).

This research has made use of data obtained from the *Chandra Data Archive* and the *Chandra Source Catalog*, and software provided by the Chandra X-ray Center (CXC) in the application packages CIAO and Sherpa.

This work has made use of data from the European Space Agency (ESA) mission *Gaia* (<https://www.cosmos.esa.int/gaia>), processed by the *Gaia* Data Processing and Analysis Consortium (DPAC, <https://www.cosmos.esa.int/web/gaia/dpac/consortium>). Funding for the DPAC has been provided by national institutions, in particular the institutions participating in the *Gaia* Multilateral Agreement.

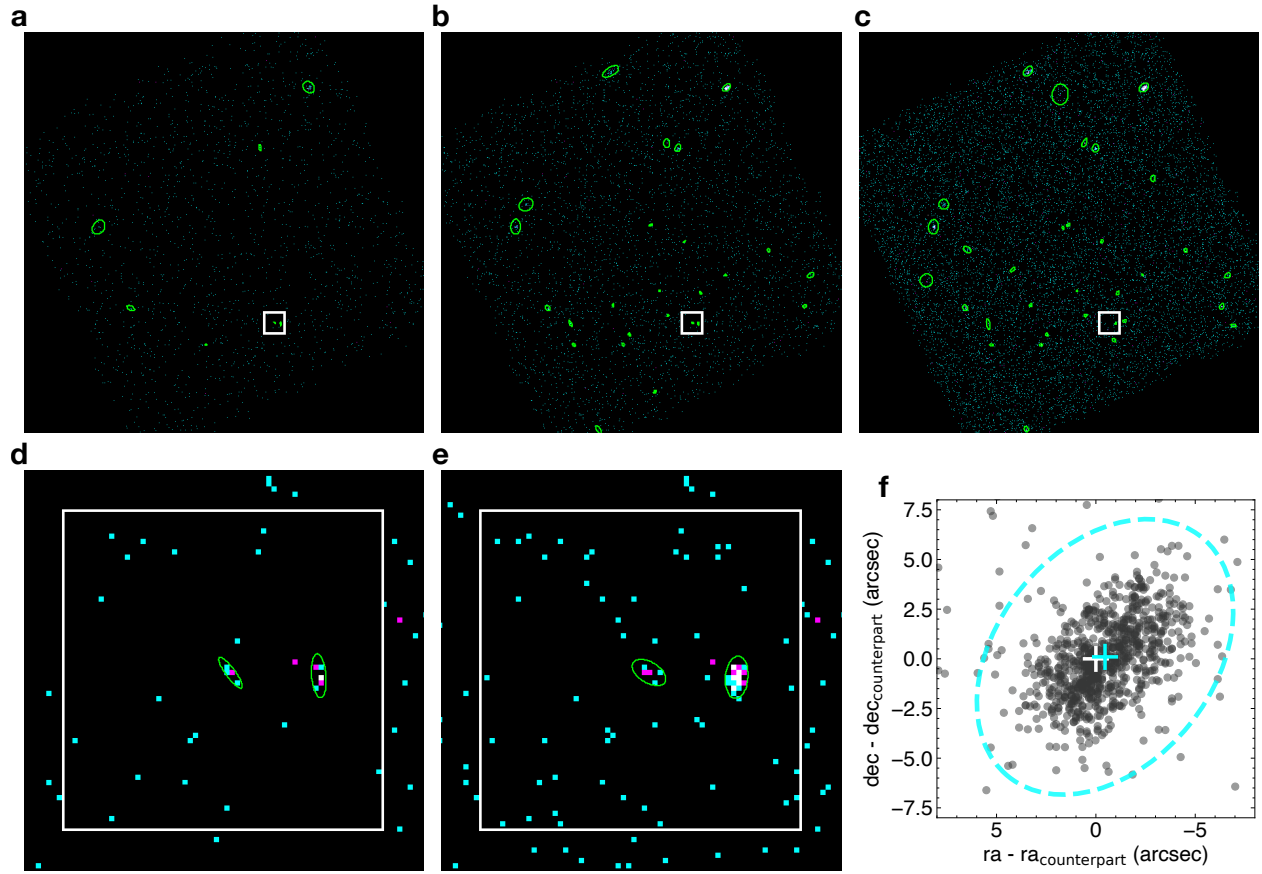
The Pan-STARRS1 Surveys (PS1) and the PS1 public science archive have been made possible through contributions by the Institute for Astronomy, the University of Hawaii, the Pan-STARRS Project Office, the Max-Planck Society and its participating institutes, the Max Planck Institute for Astronomy, Heidelberg and the Max Planck Institute for Extraterrestrial Physics, Garching, The Johns Hopkins University, Durham University, the University of Edinburgh, the Queen’s University Belfast, the Harvard-Smithsonian Center for Astrophysics, the Las Cumbres Observatory Global Telescope Network Incorporated, the National Central

University of Taiwan, the Space Telescope Science Institute, the National Aeronautics and Space Administration under Grant No. NNX08AR22G issued through the Planetary Science Division of the NASA Science Mission Directorate, the National Science Foundation Grant No. AST-1238877, the University of Maryland, Eotvos Lorand University (ELTE), the Los Alamos National Laboratory, and the Gordon and Betty Moore Foundation.

**Author contributions** T.C. performed most of the data analysis and led the writing of the manuscript. P.J.W. contributed to the original observing proposal, the data analysis and the writing of the manuscript. P-E.T and B.T.G. contributed to the writing of the manuscript and discussions on the various constraints on accretion rates. G.W.K., O.T. and D.V. contributed to the original observing proposal and to discussions throughout the project.

**Author Information** Reprints and permissions information is available at [www.nature.com/reprints](http://www.nature.com/reprints). Correspondence and requests for materials should be addressed to T.C. (email: [timothy.cunningham@warwick.ac.uk](mailto:timothy.cunningham@warwick.ac.uk)).

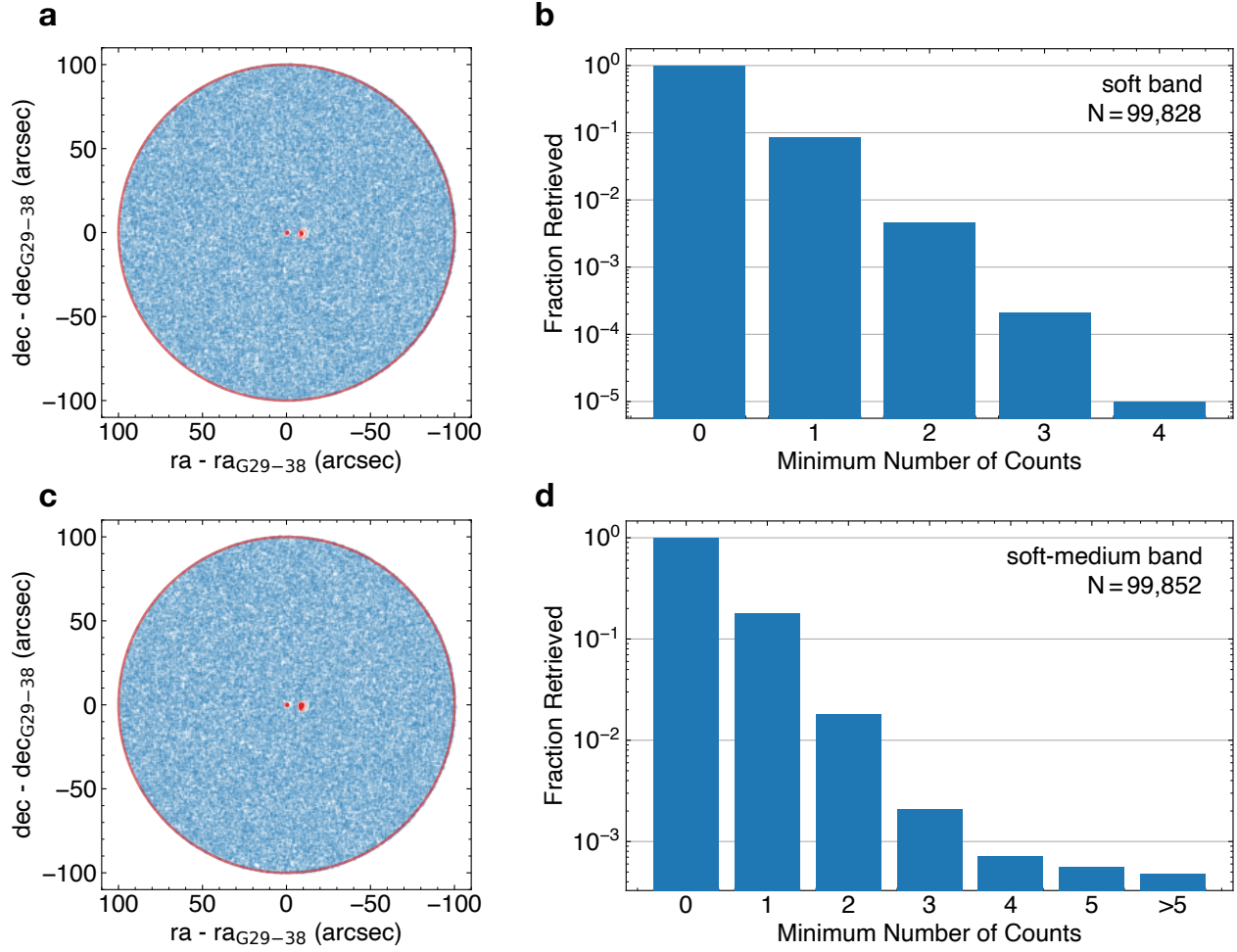
**Competing Interests** The authors declare that they have no competing interests.



**Extended Data Fig. 1 | Estimate of sky density from a source detection algorithm.**

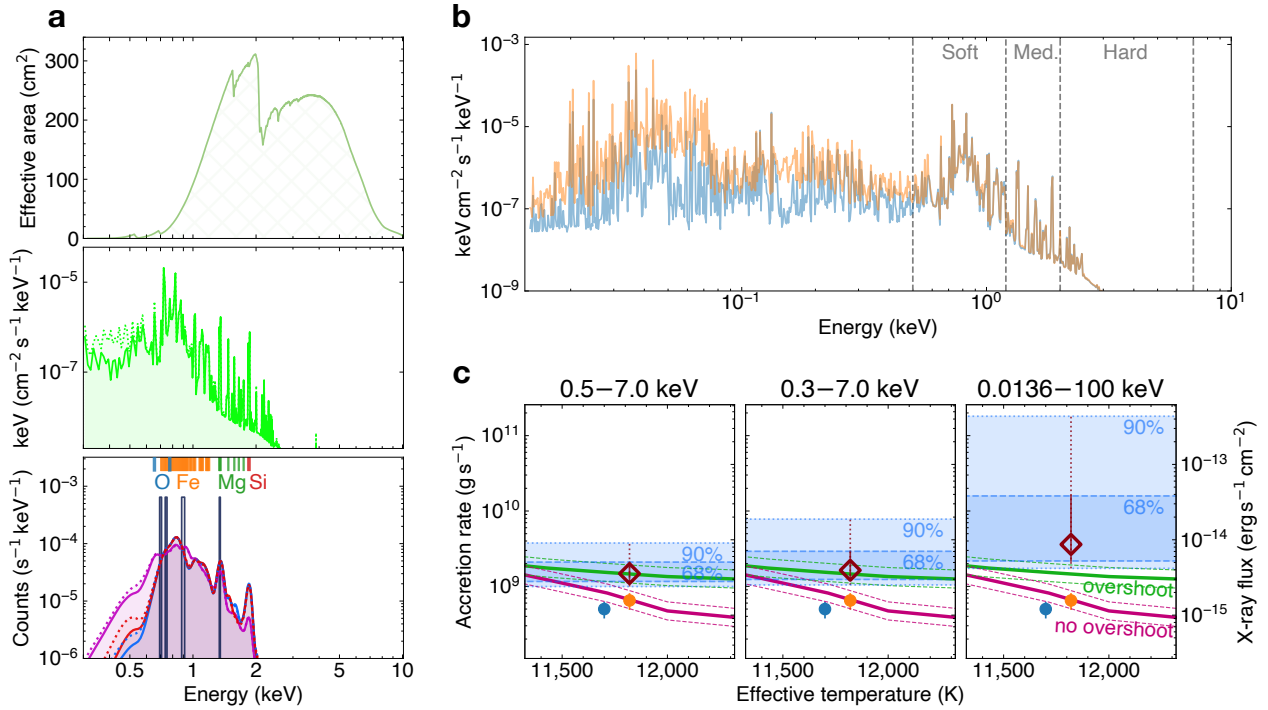
Output of the `wavdetect` source detection algorithm using the recommended significance threshold, `sigthresh`, of  $s_1 = 10^{-6}$ . **a, b & c**, are the results for the science bands used in this study; soft, soft+medium and broad, respectively, with 1, 2, and 3 counts shown in cyan, magenta, and white, respectively. **a–c** show the full field of view of the S3 chip on ACIS-S with sources identified by `wavdetect` shown in green. **d & e**, give a magnified view of the vicinity near the target for the soft and soft+medium bands respectively, where the white square has sides of length 30 arcsec and is centered on the target coordinates. The source at the sky location of G29–38 is detected in the soft and soft+medium

band images. The number of sources and corresponding sky density for each band can be found in Extended Data Table 3. **f**, Broadband (0.5–7.0 keV) events recorded near the sky position of the only *Gaia* source (EDR3 source ID: 2661110815469507072) in the full CCD image which has a detected X-ray source in the broadband image within 5 arcsec. The output of `wavdetect` gives the coordinates for the center of the detected source in (RA, DEC) as  $(352.182358 \pm 0.000022, +5.341529 \pm 0.000020)$ , shown in the figure with a cyan cross. The coordinates of the *Gaia* EDR3 source, corrected for proper motion, are  $(352.18248533 \pm 0.00000007, +5.34150200 \pm 0.00000008)$ , indicated in the figure with a white cross. The *Chandra* source is offset compared to the expected *Gaia* position by  $(-0.46 \pm 0.08, 0.10 \pm 0.07)$ , which is consistent with the offset of our target from the expected position (see Fig. 2).



**Extended Data Fig. 2 | Monte Carlo aperture photometry.** **a & c**, The blue points show the positions of the  $\approx 100,000$  test apertures, each 1 arcsec in radius, used to sample 52 arcsec around the target. The absolute number of test apertures, after removing those that fell within a masked region, is shown in the panels. The sky coordinates of all recorded events that fall within a masked region are shown in orange. **b & d**, The normalised histogram shows the fraction of test apertures with event counts equal to or greater than that of a given bin. The Monte Carlo was performed on the soft (**a–b**) and soft+medium (**c–d**) bands. The soft band analysis has 0.001% of test apertures returning

four counts, allowing us to rule out chance alignment at  $4.4\sigma$ .

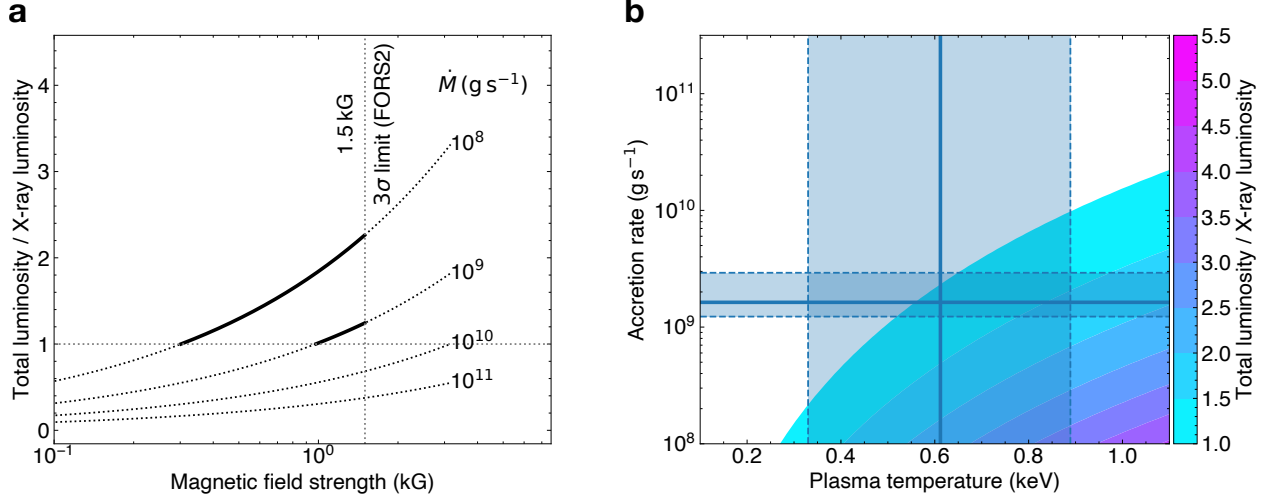


**Extended Data Fig. 3 | Spectral modelling of observed X-ray events.** **a**, Bottom, in units of instrumental counts we show the five recorded events (black) and six best-fit spectral models assuming Solar<sup>39</sup> (magenta), bulk Earth<sup>40</sup> (blue) and photospheric<sup>17</sup> (red) abundances, with either the `vvapec` isothermal (solid) and `mkcflow` cooling flow (dotted) plasma models. We also indicate the dominant metal emission lines (O, Mg, Si and Fe) from the isothermal, photospheric abundance model. Middle, in real flux units, we show the synthetic spectra for the photospheric abundances with the isothermal (solid) and cooling flow (dotted) plasma models. The modelling suggests the most likely origin of the source photon at 1.3 keV was a Mg transition. Top, the effective area of the ACIS-S detector is shown in green, hatch. The absence of harder X-ray events ( $>2.0$  keV) in

the *Chandra* observations demonstrates that the plasma emission spectrum is very soft.

**b**, Spectral energy distribution of the best-fit isothermal (blue) and cooling flow (orange) plasma models with bulk Earth abundances down to the extreme ultraviolet (EUV) energy regime. Also shown are the standard *Chandra* science bands; soft, medium and hard. Both models provide a convergent fit within the *Chandra* ACIS-S passband, but the cooling flow provides a more physical and larger estimate of the lower-energy flux.

**c**, The X-ray flux measured in 3 bands: 0.5–7.0 keV, 0.3–7.0 keV and 0.0136–100 keV, using the cooling flow model for the photospheric abundances<sup>17</sup> is shown in open diamonds. The filled horizontal bands show the 68% and 90% confidence intervals on the X-ray accretion rate, which is computed using Equation (1). The X-ray accretion rates are computed using Equation (1), with  $A = 1$ ,  $R_{\text{WD}} = 0.0129R_{\odot}$ , and  $M_{\text{WD}} = 0.6M_{\odot}$ . The spectroscopic accretion rates (solid lines) are the same as shown in Fig. 3, with the  $1\sigma$  uncertainty shown with dashed lines. Also shown in solid circles (blue and orange) are the previously published inferred accretion rates for G29–38, based on photospheric abundances from spectroscopic observations<sup>17,28</sup>.



**Extended Data Fig. 4 | Limit on cyclotron emission cooling as source of additional luminosity.** **a**, An estimate for the total luminosity from the measured X-ray luminosity, accounting for cyclotron emission cooling. We compare the measured plasma temperature,  $kT_X = (0.61 \pm 0.28) \text{ keV}$ , given by the cooling flow model and photospheric abundances, with the critical plasma temperature,  $T_B$ , above which cyclotron emission cooling dominates, defined by equation 10 from ref.<sup>22</sup>. The authors provide the ratio  $T_X/T_B \approx L_{\text{tot}}/L_X$  as an estimate of, for a range of accretion rates and global magnetic field strengths, the predicted increase in total luminosity compared to X-ray luminosity if the plasma temperature is sufficient to be dominated by cyclotron emission cooling. The horizontal dotted line indicates  $T_X/T_B = 1$ , where no correction is expected below this. The vertical dotted line indicates the 3 $\sigma$  upper limit on the magnetic field strength from FORS2 spectropolarimetric observations<sup>22</sup>. The solid lines indicate the increase in total luminosity when compared to the observed X-ray luminosity. **b**, Predicted additional luminosity for an assumed global magnetic field at the 3 $\sigma$  limit (1.5 kG) across the full range of plasma temperatures and



accretion rates calculated in this work (see Extended Data Tables 5 & 6). White space indicates no additional luminosity. The upper plasma temperature from the cooling flow model and accretion rate derived from the isothermal plasma model is shown (solid) along with the 68% uncertainty (dashed). Even at the observational upper limit, the predicted increase due to cyclotron emission cooling is a factor of  $1.1^{+0.6}_{-0.1}$ .

**Extended Data Table 1 | *Chandra* observations of G29–38.**

Obs ID	Instrument	Exposure Time (ks)	Start Date (yyyy-mm-dd)	Epoch (yr)
24257	ACIS-S	24.58	2020-09-22	J2020.727
24256	ACIS-S	14.89	2020-09-24	J2020.732
24658	ACIS-S	14.89	2020-09-24	J2020.732
23379	ACIS-S	26.23	2020-09-26	J2020.738
24657	ACIS-S	25.74	2020-09-27	J2020.740
Total:	–	106.33	–	–

Details of *Chandra* observations carried out between 22 and 27 September 2020 with G29–28 as the target (PI: Cunningham).

**Extended Data Table 2 | Statistical significance of source detection.**

Band	Energy (keV)	Source (per ap.)	Background		CL		Significance	
			(per ap.)		(% )		$(\sigma)$	
			$r_{1.0}$	$r_{0.5}$	$r_{1.0}$	$r_{0.5}$	$r_{1.0}$	$r_{0.5}$
Soft	0.5–1.2	4	0.100	0.025	99.99962	99.9999984	4.62	5.65
Soft+Medium	0.5–2.0	5	0.205	0.051	99.99975	99.9999997	4.71	5.94
Broad	0.5–7.0	5	0.566	0.142	99.97255	99.9999590	3.64	5.06

Source counts ( $N$ ) and expected background ( $b$ ) in the three standard ACIS energy bands used in this study, given in units of counts per 1 arcsec aperture ( $r_{1.0}$ ). From top to bottom, the total background counts in each band was  $N_b=270$ , 555 and 1530 (in the 52 arcsec radius background region). The expected background in the 1 arcsec radius source region was thus computed as  $b = N_b/52^2$ . This includes reprocessing using the `VFAINT` mode for background cleaning. For an expected background,  $b$ , the Poisson distribution gives the probability of receiving  $N$  or more counts as  $P(N|b) = b^N e^{-b}/(N!)$ . We therefore reject the null hypothesis of detecting no source photons with a confidence of  $\text{CL} = 100 \times (1 - P(N|b))$ . We also provide results for the relocalised 0.5 arcsec aperture ( $r_{0.5}$ ), and note that the source counts are the same for both aperture sizes.

**Extended Data Table 3 | Sky density of sources from the `wavdetect` source detection algorithm.**

Band	No. Sources		Target?		Sky Density ( $10^{-5} \text{ arcsec}^{-2}$ )		$CL_{\text{align}}$ (%)	Significance ( $\sigma$ )
	$s_1$	$s_2$	$s_1$	$s_2$	$s_1$	$s_2$	$s_1$	$s_1$
Soft	7	6	✓	×	2.36	2.36	99.996	4.1
Soft+Medium	25	23	✓	✓	9.46	8.76	99.985	3.8
Broad	32	32	×	×	12.6	12.6	99.979	3.7

We present results in each of the three standard science bands considered (soft, soft+medium and broad), for two values of the significance threshold parameter, `sigthresh`, where  $s_1$  and  $s_2$  are significance thresholds of  $1 \times 10^{-6}$  and  $5 \times 10^{-7}$ . From the documentation, the significance threshold should be set to  $s = 1/n_{\text{px}}$ , which typically produces one false detection. The ACIS-S S3 CCD has  $1024 \times 1024$  pixels, so  $s_1$  should be a sufficiently low threshold. However, to align with the world coordinate system (WCS), the CCD image is rotated relative to the bounding box of the image, meaning that the image on which `wavdetect` was run has  $1414 \times 1401$  pixels, hence the value of  $s_2 = 1/(1414 \times 1401) \approx 5 \times 10^{-7}$ . The sky density is computed as the number of sources (excluding the target, if detected), divided by the field of view, which is estimated as  $(1024^2 \times 0.4920^2)$ , where the second number is the pixel size in arcsec. Multiplying the sky density by the area defined by the 90% confidence limit on the radial offset of ACIS-S targets ( $\pi 0.72^2 \text{ arcsec}^2$ ), we provide the confidence,  $CL_{\text{align}}$ , with which we can reject the hypothesis that our source counts could originate from a background source.

**Extended Data Table 4 | Confidence interval on *Chandra* ACIS-S count rate.**

Band	Energy (keV)	Count rate (ap. <sup>-1</sup> ks <sup>-1</sup> )					
		Source	Background	68%		90%	
				low	high	low	high
Soft	0.5–1.2	0.038	0.0010	0.021	0.059	0.013	0.078
Soft+Medium	0.5–2.0	0.047	0.0021	0.027	0.070	0.018	0.090
Broad	0.5–7.0	0.047	0.0057	0.024	0.066	0.015	0.086

The 68% and 90% confidence intervals for the source counts ( $N$ ) given in Extended Data Table 2, which have been converted to a count rate using the 106.33 ks total exposure time for the three standard *Chandra* energy bands used in this study. Confidence intervals are calculated using the method of ref.<sup>34</sup>, which is a Bayesian approach to Poisson statistics in the presence of a background that uses a simple prior on the number of source counts not being negative. All count rate values are given in units of counts per ks, per 1 arcsec aperture.

**Extended Data Table 5 | Plasma temperature from spectral modelling using XSPEC.**

Abundance	Model	Plasma Temperature (keV)				
		Best-fit	68%		90%	
			low	high	low	high
Solar <sup>31</sup>	Isothermal	0.273	0.198	0.401	0.165	0.653
	Cooling flow	<b>0.317</b>	0.226	0.581	0.187	0.922
Bulk Earth <sup>40</sup>	Isothermal	0.473	0.231	0.653	0.172	0.772
	Cooling flow	<b>0.594</b>	0.273	0.882	0.193	1.107
Photospheric <sup>17</sup>	Isothermal	0.491	0.283	0.661	0.185	0.778
	Cooling flow	<b>0.612</b>	0.330	0.889	0.210	1.111

The 68% and 90% confidence intervals for the derived plasma temperature are based on fits to the full ACIS-S spectrum (plotted in Extended Data Figure 3). Best fits and confidence intervals were determined using the C-statistic,<sup>42</sup> and with no background subtraction. For the cooling flow model these are the upper temperature of a range of temperatures extending down to 0.08 keV, with the emission measure at each temperature weighted by the inverse of the emissivity.

**Extended Data Table 6 | Best-fit X-ray properties of G29–38.**

X-ray measurement	Energy (keV)	Best-fit	68%		90%	
			low	high	low	high
Flux ( $10^{-15}$ erg s $^{-1}$ cm $^{-2}$ )	0.5–7.0	<b>1.78</b>	1.40	2.53	1.20	4.53
	0.3–7.0	<b>1.97</b>	1.49	3.52	1.26	9.40
	0.0136–100	<b>4.34</b>	2.62	19.1	2.09	218.0
Luminosity ( $10^{25}$ erg s $^{-1}$ )	0.5–7.0	<b>6.54</b>	5.15	9.30	4.41	16.7
	0.3–7.0	<b>7.24</b>	5.48	12.9	4.63	34.5
	0.0136–100	<b>16.0</b>	9.63	70.2	7.68	801.3
Accretion rate ( $10^9$ g s $^{-1}$ )	0.5–7.0	<b>1.48</b>	1.16	2.09	1.00	3.76
	0.3–7.0	<b>1.63</b>	1.23	2.92	1.05	7.80
	0.0136–100	<b>3.60</b>	2.17	15.8	1.73	181

The best-fit fluxes are computed across three spectral energy ranges using the cooling flow model with photospheric abundances<sup>17</sup>. The first two energy ranges are within the wavelength range of our observations and provide a robust lower limit on the flux. The third, wider energy band allows for more flux to be carried at higher and lower energies, thus providing an upper estimate of the X-ray flux based on our observations. The 68% and 90% confidence intervals for the derived flux based on those for the plasma temperature in Extended Data Table 5. From the fluxes ( $F_X$ ), the best-fit X-ray luminosity ( $L_X$ ) was derived using  $L_X = 4\pi d^2 F_X$ . The best-fit X-ray accretion rate ( $\dot{M}_X$ ) derived using  $\dot{M}_X = 2L_X R_{WD}/(GM_{WD})$ .